



**HAL**  
open science

## Rapidly rotating spherical Couette flow in a dipolar magnetic field: an experimental study of the mean axisymmetric flow

Henri-Claude Nataf, Thierry Alboussiere, Daniel Brito, Philippe Cardin, Nadège Gagnière, Dominique Jault, Denys Schmitt

### ► To cite this version:

Henri-Claude Nataf, Thierry Alboussiere, Daniel Brito, Philippe Cardin, Nadège Gagnière, et al.. Rapidly rotating spherical Couette flow in a dipolar magnetic field: an experimental study of the mean axisymmetric flow. *Physics of the Earth and Planetary Interiors*, 2008, 170, pp.60-72. 10.1016/j.pepi.2008.07.034 . insu-00143935v2

**HAL Id: insu-00143935**

**<https://insu.hal.science/insu-00143935v2>**

Submitted on 8 Aug 2008

**HAL** is a multi-disciplinary open access archive for the deposit and dissemination of scientific research documents, whether they are published or not. The documents may come from teaching and research institutions in France or abroad, or from public or private research centers.

L'archive ouverte pluridisciplinaire **HAL**, est destinée au dépôt et à la diffusion de documents scientifiques de niveau recherche, publiés ou non, émanant des établissements d'enseignement et de recherche français ou étrangers, des laboratoires publics ou privés.

# Rapidly rotating spherical Couette flow in a dipolar magnetic field: an experimental study of the mean axisymmetric flow

Nataf, H.-C. \* Alboussière, T., Brito, D., Cardin, P.,  
Gagnière, N., Jault, D., and Schmitt, D.

*Geodynamo team, LGIT-UMR5559-CNRS-UJF, Grenoble, France*

---

## Abstract

In order to explore the magnetostrophic regime expected for planetary cores, in which the Lorentz forces balance the Coriolis forces, experiments have been conducted in a rotating sphere filled with liquid sodium, with an imposed dipolar magnetic field (the *DTS* setup). The field is produced by a permanent magnet enclosed in an inner sphere, which can rotate at a separate rate, producing a spherical Couette flow. The flow properties are investigated by measuring electric potentials on the outer sphere, the induced magnetic field in the laboratory frame just above the rotating outer sphere, and velocity profiles inside the liquid sodium using ultrasonic Doppler velocimetry. The present article focuses on the time-averaged axisymmetric part of the flow. The electric potential differences measured at several latitudes can be linked to azimuthal velocities, and are indeed found to be proportional to the azimuthal velocities measured by Doppler velocimetry. The Doppler profiles show that the angular velocity of the fluid is relatively uniform in most of the fluid shell, but rises near the inner sphere, revealing the presence of a “magnetic wind”, and gently drops towards the outer sphere. The transition from a magnetostrophic flow near the inner sphere to a geostrophic flow near the outer sphere is controlled by the local Elsasser number. For Rossby numbers up to order 1, the observed velocity profiles all show a similar shape. Numerical simulations in the linear regime are computed, and synthetic velocity profiles are compared with the measured ones. A good agreement is found for the angular velocity profiles. In the geostrophic region, a torque-balance model provides very good predictions. Radial velocities change sign with the Rossby number, as expected for an Ekman-pumping dominated flow. For a given Rossby number the amplitude of the measured angular velocity is found to vary by as much as a factor of 3. Comparison with numerical simulations suggests that this is due to variations in the electric coupling between liquid sodium and the inner copper sphere, implying an effect equivalent to a reduction of the inner sphere electric conductivity by as much as a factor 100. We show that the measured electric potential difference can be used as a proxy of the actual fluid velocity. Using this proxy in place of the imposed differential velocity, we find that the induced magnetic field varies in a consistent fashion, and displays a peculiar peak

in the counter-rotating regime. This happens when the fluid rotation rate is almost equal and opposite to the outer sphere rotation rate. The fluid is then almost at rest in the laboratory frame, and the Proudman-Taylor constraint vanishes, enabling a strong meridional flow. We suggest that dynamo action might be favored in such a situation.

*Key words:* Spherical Couette flow, magnetostrophic, liquid sodium experiment, dynamo, Taylor-state, ultrasonic Doppler velocimetry.

*PACS:* 47, 47.65, 91, 91.25

---

## 1 Introduction

The internal dynamics of liquid planetary cores is deeply influenced by the rotation of the planet and (in many cases) by the presence of a magnetic field, and can be in the so-called magnetostrophic regime where the Coriolis and Lorentz forces balance each other. In recent years, attention has been paid to the rotating spherical Couette flow in the presence of a magnetic field (Kleeorin et al., 1997; Hollerbach, 1994; Dormy et al., 1998; Starchenko, 1998; Hollerbach, 2000; Nataf et al., 2006). An electrically conducting liquid fills the gap between two concentric spheres and is sheared through the differential rotation of the two spheres. A magnetic field can be applied. This flow has the distinct advantage of being amenable to both experiments and numerical models, while retaining important ingredients of natural situations. Numerical simulations (Dormy et al., 1998; Hollerbach, 2000) and asymptotics (Kleeorin et al., 1997; Starchenko, 1998; Dormy et al., 2002) highlight the importance of the magnetic wind that arises when the magnetic field lines are not parallel to the rotation axis, as for a dipolar field. This magnetic wind can entrain the fluid at angular velocities larger than that of the inner sphere, a phenomenon called super-rotation (Dormy et al., 1998, 2002). The rotating spherical Couette flow has also been proposed for producing a dynamo (Cardin et al., 2002). Numerical models have shown that dynamo action could be produced this way, even in liquids with a low magnetic Prandtl number, such as liquid metals (Schaeffer and Cardin, 2006). This has led Dan Lathrop and his team to build a 3m-diameter sphere with a rotating inner sphere in the hope of starting a dynamo, once the gap is filled with liquid sodium and the differential rotation is large enough.

---

\* corresponding author

*Email address:* Henri-Claude.Nataf@ujf-grenoble.fr (Nataf, H.-C.).

*URL:*

<http://www-lgit.obs.ujf-grenoble.fr/recherche/geodynamo/Epage.html>  
(Nataf, H.-C.).

Here, we report on results obtained in the *DTS* (*Derviche Tourneur Sodium*) experiment. This experiment, described in Cardin et al. (2002) and Nataf et al. (2006), is a rotating spherical Couette flow with an imposed axisymmetric dipolar magnetic field. Because of this strong imposed field, and although liquid sodium is used, the dynamo effect cannot be studied in the *DTS* experiment. However, it permits to explore very similar dynamics. In particular, the magnetic field is large enough to strongly influence the flow (interaction parameter  $N$  up to 200) and the magnetic field is strongly affected by the flow (magnetic Reynolds number  $Rm$  up to 44).

This kind of experiment can bring information on the level and organization of turbulence in situations where both rotation and the magnetic field impose strong constraints on the flow. Local theories have been proposed (Braginsky and Meytlis, 1990), partly backed by numerical simulations (St. Pierre, 1996), and some teams are trying to implement sub-grid models based on these theories in full dynamo models (Buffett, 2003; Matsui and Buffett, 2007). Results obtained in the *DTS* experiment suggest an alternative view, in which waves play a major role (Schmitt et al., 2008). A good characterization of the mean axisymmetric flow is needed in order to fully exploit these observations.

An experimental setup, built by Dan Lathrop and his group (Sisan et al., 2004; Kelley et al., 2007) is very similar to our *DTS* experiment. The main difference is that an axial magnetic field is applied by external coils in Sisan et al. (2004) and Kelley et al. (2007), while we impose a strong dipolar magnetic field in *DTS* since the inner sphere contains a permanent magnet. One of the consequences is that the entrainment of the conducting fluid is much stronger, since the inner sphere acts as a magnetic stirrer. We also have developed specific instrumentation, such as measuring the electric potential at the surface of the outer sphere, which carries important information on the flow (Nataf et al., 2006; Schmitt et al., 2008).

In this article, we focus on the time-averaged axisymmetric magnetohydrodynamic flow observed in *DTS* when the outer sphere rotates. The first observations were described in Nataf et al. (2006), and more thorough results for a static outer sphere will be discussed in a forthcoming article.

Nataf et al. (2006) showed that the measurement of electric potential differences at the surface of the outer sphere could be related to the azimuthal velocity of the liquid beyond the Hartmann boundary layer. It was found that this velocity could be larger than the solid-body rotation of the inner sphere, providing experimental evidence for the so-called super-rotation predicted by Dormy et al. (1998). However, the latitudinal variation of the electric potential differences was found to differ markedly from the one calculated in a linear numerical model, analogous to that of Dormy et al. (1998). The relative variation of electric potential differences with latitude turned out to be

universal, independent of the differential rotation of the inner sphere. This was particularly true when the outer sphere was at rest. The electric design of the electrodes and acquisition system has been improved since, yielding better quality signals.

Numerical models provide a useful guide for interpreting the experimental observations. Linear solutions have been computed by Dormy et al. (1998) for a situation similar to ours (spherical Couette with an imposed dipolar magnetic field, a conducting inner sphere and a rapidly rotating outer sphere). The results show that as the magnetic field is increased, the flow evolves from the classical Stewartson solution (Stewartson, 1966), with a cylindrical shear-layer attached to the rotating inner sphere, to a solution where the fluid enclosed within a closed magnetic field line is entrained by the inner sphere to angular velocities in excess of the imposed differential rotation. A shear-layer develops around that field line (Dormy et al., 2002). Using the numerical approach described in Nataf et al. (2006), we have extended these computations to conditions closer to the actual *DTS* configuration, with stronger global ( $f$ ) and differential ( $\Delta f$ ) rotation rates. The results are presented in figure 1. The angular velocity contours (figure 1a) clearly illustrate the existence of two domains: a region close to the inner sphere where the magnetic effects dominate, and a region where the flow is geostrophic farther away. In the inner region, the angular velocity contours follow the magnetic field lines (Ferraro law of isorotation (Ferraro, 1937)), while they are aligned with the rotation axis in the geostrophic region. Dormy et al. (1998) demonstrate that the radial extent of the magnetic-dominated region solely depends upon the Elsasser number (which compares the Lorentz and Coriolis forces). In contrast to the Stewartson solution, the bulk of the fluid is entrained by the inner sphere, and a thin Ekman-Hartmann layer forms beneath the outer shell. Ekman pumping results and feeds the meridional circulation shown in figure 1b. The circulation around the main vortex is counterclockwise in the upper hemisphere (*i.e.* centrifugal at the equator) when the inner and outer spheres rotate in the same direction, and clockwise (*i.e.* centripetal at the equator) when the two spheres are in contra-rotation. The field lines of the meridional magnetic field produced by this circulation are drawn in figure 1c.

Direct measurements of the flow velocity were presented in Nataf et al. (2006), using ultrasonic Doppler velocimetry, but only radial profiles of the radial velocity could be obtained. More profiles are now available and can be compared with the numerical simulations. The setup now permits the record of profiles of the angular velocity as well, revealing the actual variation of angular velocity inside the sphere. We will see that they confirm the progressive rise of the angular velocity from the equator of the outer sphere to the interior of the fluid predicted by the numerical simulations (figure 1a). The existence of this peculiar boundary layer was predicted by Kleorin et al. (1997). We will present their approach and propose an extension that provides a better fit to

our observations.

There were some hints in Nataf et al. (2006) that different flows could be observed for the same imposed velocities. With additional data now available, this tendency is fully confirmed. We think that this is due to variations in the electric coupling between the liquid sodium and the copper inner sphere. Indeed, the entrainment of the liquid is not viscous but depends on electric currents that flow between the liquid sodium and the copper shell of the inner sphere. The presence of oxides or other impurities, or imperfect wetting on that shell can hinder the electric currents. However, we show in this article that we can use the difference in electric potentials at one latitude (40° for example) as a proxy of the actual differential angular velocity of the fluid, and get a much more coherent picture of the various observations, if we relate them to this actual value.

No measurement of the induced magnetic field was provided by Nataf et al. (2006). Here, we present measurements of the radial and orthoradial components of the induced magnetic field at a latitude of about 50° just outside the outer sphere, in the laboratory frame. The mean values correspond to the field induced by the mean meridional flow. When the outer sphere is rotating, a very peculiar behavior is monitored for a particular counter-rotation rate of the inner sphere.

We recall the main features of the *DTS* setup and measuring techniques in section 2. The typical dimensionless numbers are discussed in section 3. The results are presented in section 4, and discussed in section 5.

## 2 Experimental setup and measuring techniques

### 2.1 Setup

The central part of the *DTS* experiment is sketched in figure 2. Forty liters of liquid sodium are contained between an inner sphere of radius  $b = 7.4$  cm and an outer spherical surface of radius  $a = 21$  cm. The 5 mm-thick outer sphere is made of stainless steel, which is 8 times less electrically conductive than sodium at 130°C, the typical experimental temperature. The inner sphere is made of two hollow copper hemispheres filled with 5 layers of magnetized rare-earth cobalt bricks. Copper is about 4.2 times more conductive than sodium. Outside the copper sphere, the magnetic field is found to be an axial dipole, aligned with the axis of rotation and pointing downwards with:

$$\vec{B}(r, \theta) = \frac{\mu_0 \mathcal{M}}{4\pi r^3} (2\vec{e}_r \cos \theta + \vec{e}_\theta \sin \theta),$$

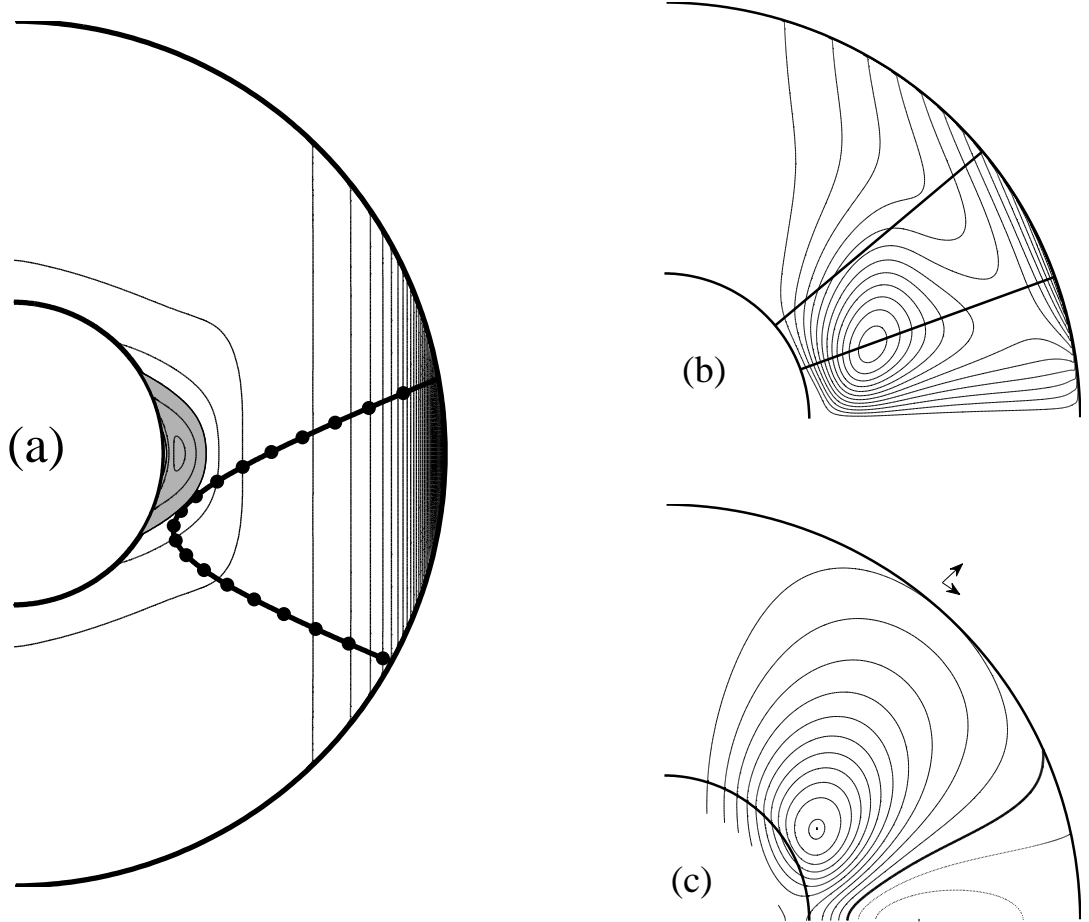


Fig. 1. Non-linear axisymmetric numerical simulation with the geometry and parameters of the *DTS* setup, corresponding to  $f = 5$  Hz and  $\Delta f = 0.4$  Hz (see section 3 below) (a) Contour map of the angular velocity. The interval between contours is 0.027 in  $2\pi\Delta f$  units. Angular velocities are larger than that of the inner sphere in the shaded region (super-rotation). Two different regions are clearly visible: the region near the inner sphere, where the flow lines are aligned with the magnetic field lines of the imposed dipole (Ferraro law), and where the angular velocity exceeds that of the inner sphere by up to 6%; farther away, a region where the flow is nearly geostrophic, with contours aligned with the rotation axis (vertical). Also drawn, the trajectory of the ultrasonic beam shot from the “azimuthal” assembly at  $+10^\circ$ , projected on the meridional plane. Marks are drawn every 2 cm along the ray path. (b) Meridional circulation. The interval between contours is  $2.7 \times 10^{-5}$  in  $2\pi a^2 \Delta f$  units, where  $a$  is the radius of the outer sphere. The main circulation is counterclockwise, *i.e.* centrifugal at the equator. It changes sign with  $\Delta f$ . Radial velocities are measured along radial shots at latitudes  $40^\circ$  and  $20^\circ$  (lines). (c) Field lines of the induced meridional magnetic field. The interval between contours is  $2 \times 10^{-3}$  in  $aB_0$  units.  $B_0$  is the intensity of the imposed dipolar magnetic field at the equator at the outer sphere. The 0 line is thicker. While the imposed dipole is pointing downwards, the induced field points up at high latitudes.  $B_r$  and  $B_\theta$  are measured at a latitude of  $50^\circ$ , 1 cm away from the sodium boundary (arrows).

in spherical coordinates, with  $\theta$  the colatitude and  $\mathcal{M} = -700 \text{ Am}^2$  the magnetic dipolar moment, yielding a magnetic field amplitude ranging from 0.345 T at the poles of the inner sphere down to 0.008 T at the equator of the outer sphere. More details are given in Nataf et al. (2006).

The inner and outer spheres are set in rotation around the vertical axis. In this article, we present results obtained for imposed rotation rates  $f$  of the outer sphere of 5, 10 and 15 Hz. The rotation rate of the inner sphere in the laboratory frame is varied between -25 and +25 Hz, yielding differential rotation rates  $\Delta f$  of the inner sphere in the rotating frame ranging from -40 to 20 Hz (depending upon  $f$ ). Each sphere is entrained by an 11 kW brushless electric motor (Yaskawa SGMGH-1ADCA61).

The torques and actual rotation rates are retrieved as analog signals from the two motor controllers. In order to decipher the organisation of the flow in the liquid, several techniques are employed. Electric potentials are measured at several locations on the outer sphere. Profiles of the flow velocity are obtained using ultrasonic Doppler velocimetry. Since the outer sphere is rotating, all these signals must pass through electric slip-rings to be analyzed in the laboratory frame. We use a 36-tracks 10A slip-ring system (Litton AC6275-12). In order to decrease electromagnetic perturbations of the signals, this system is completely enclosed in an aluminum casing. In contrast, the magnetic field is measured in the laboratory frame, with magnetometer sensors a few millimeters away from the rotating surface of the outer sphere.

## 2.2 *Electric potentials*

We measure the electric potential at several points on the outer sphere. Blind holes are drilled in the 5 mm-thick stainless steel shell. The holes are 1 mm in diameter, and 4 mm-deep. They are threaded and equipped with 3 mm-long M1.2 mm brass bolts, on the head of which electrodes are soldered. Stainless steel is a poor electric conductor as compared to liquid sodium and thus it does not affect the dynamically generated electric potential, but it is a good enough electric conductor for the impedance of electrode pairs to be much smaller than that of the acquisition system. The measurements are acquired at 1 kHz with a PXI-6229 National Instruments board, after going through a simple anti-aliasing 215 Hz low-pass RC filter. As we focus here on the mean axisymmetric state, these data are time-averaged over time-windows ranging from 0.1 to 1 second, in order to remove fluctuations.

In this article, we present data for the difference in electric potential measured between electrodes placed along the same meridian. These electrodes are  $10^\circ$  apart and range from  $-45^\circ$  to  $+45^\circ$  in latitude as shown in figure 2. Assuming

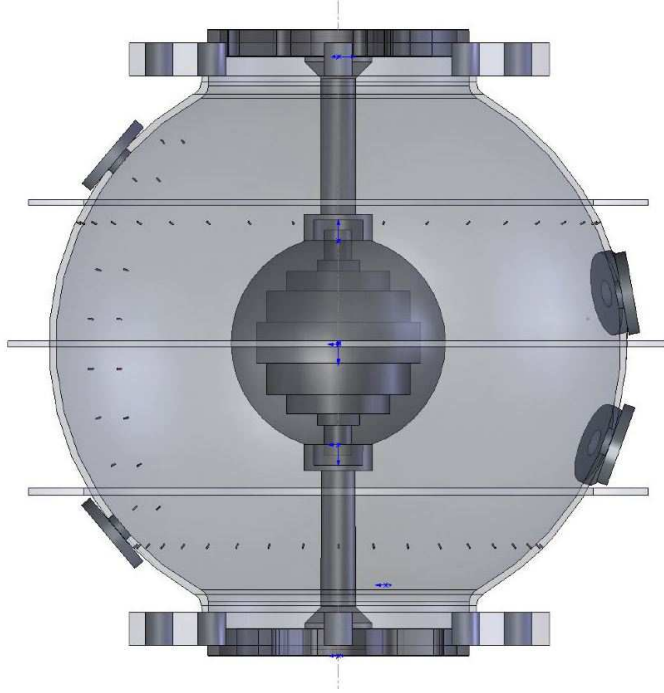


Fig. 2. Sketch of the central part of the *DTS* experiment. The 7.4 cm-radius inner sphere is made of copper and contains 5 layers of magnets. The inner radius of the stainless steel outer sphere is 21 cm and its thickness is 5 mm. Blind holes are drilled and threaded along several meridians and parallels to receive M1.2 mm brass bolts acting as electrodes. In this article, results are presented for electric potentials measured along one meridian (on the left). The large holes at latitudes  $-20^\circ$ ,  $10^\circ$  and  $\pm 40^\circ$  receive interchangeable assemblies, which can be equipped with ultrasonic transducers. Magnetometers are placed at a latitude of  $50^\circ$ , just above the outer sphere, in the laboratory frame. They measure the radial  $B_r$  and orthoradial  $B_\theta$  components of the magnetic field.

steady state, the difference in electric potential  $\Delta V$  between two electrodes separated by a latitudinal angle  $\Delta\theta$  is related to the azimuthal velocity  $U_\varphi$  of the liquid sodium by:

$$\frac{\Delta V}{a\Delta\theta} = U_\varphi B_r - \frac{j_\theta}{\sigma}, \quad (1)$$

where  $B_r$  is the radial component of the magnetic field,  $j_\theta$  is the  $\theta$ -component of the electric current, and  $\sigma$  is the electric conductivity of liquid sodium.

In Nataf et al. (2006), we used the differences in electric potential to deduce the angular velocity of the liquid sodium flow beneath the Hartmann boundary layer. Indeed, assuming that the meridional electric currents vanish below that layer, equation 1 yields:

$$U_\varphi = \frac{\Delta V}{a\Delta\theta B_r} \quad \text{or} \quad \Delta f_{\text{fluid}}(s) = \frac{\Delta V}{2\pi s a\Delta\theta B_r}, \quad (2)$$

where  $\Delta f_{\text{fluid}}(s)$  is the angular frequency of the fluid with respect to the outer sphere at the cylindrical radius  $s$  for the latitude of the electrode pair. In this article, we will use the difference in electric potential measured at  $40^\circ$  latitude ( $\Delta V_{40^\circ}$ ) as a proxy of the actual rotation frequency of the liquid sodium flow with respect to the outer sphere.

### 2.3 Ultrasonic Doppler velocimetry

Since liquid sodium is opaque, it is not possible to use optical methods to investigate the flow within the sphere. Instead, we use ultrasounds to probe the flow. Ultrasonic transducers (TR0405HS from Signal Processing, Switzerland) are placed in removable assemblies on the outer sphere, and shoot a narrow beam of 4 MHz ultrasounds. The pulsed Doppler velocimetry technique is perfectly suited for retrieving profiles of the component of the flow velocity along the shooting line, as illustrated in Brito et al. (2001), Eckert and Gerbeth (2002), and Nataf et al. (2006). We use a DOP 2000 instrument from Signal Processing, Switzerland.

While only radial profiles of the radial velocity were discussed in Nataf et al. (2006), we show here profiles of both the radial and angular velocities. Radial profiles are measured at two different latitudes ( $-20^\circ$  and  $-40^\circ$ ), as drawn in figure 1b. The angular velocities are obtained with an assembly devised for shooting a beam at an angle of  $24^\circ$  away from radial. Radial velocities are found to be at least one order of magnitude smaller than the azimuthal velocities. Neglecting the radial velocity component, the axisymmetric angular frequency  $\Delta f_{\text{fluid}}(s, z)$  of the fluid flow can thus be retrieved by projection of the velocity  $\mathcal{U}(d)$  measured along the shooting line. With our actual geometry, one gets:

$$\Delta f_{\text{fluid}}(s, z) = \frac{2.88 \mathcal{U}(d)}{2\pi a}, \quad (3)$$

where  $d$  is the distance along the shooting line,  $s$  the cylindrical radius, and  $z$  the height above the equatorial plane, which are related by:

$$z(d) = a \sin 10^\circ - 0.359 d \quad (4)$$

$$s(d) = a \cos 10^\circ \sqrt{1 - 1.76 \frac{d}{a} + 0.898 \left(\frac{d}{a}\right)^2} \quad (5)$$

As shown in figure 1a, plotting  $z$  versus  $s$  for this beam yields the projection of the ray path in a meridional plane. Tick marks have been drawn every 2

cm along the path. The minimum cylindrical radius reached is  $s = 7.7$  cm, close to the radius of the inner sphere (7.4 cm), but it is attained some 4 cm beneath the equator.

The Doppler technique relies upon ultrasonic energy backscattered by particles in the liquid. We did not add any particle in the liquid sodium. In liquid metals, it is often assumed that the backscattered echoes are due to floating oxides. It is interesting to note that we were able to record good profiles, even when the outer sphere was rotating at 14 Hz, implying centrifugal acceleration up to 180 times the acceleration due to gravity.

#### 2.4 Induced magnetic field

The magnetic field is measured outside the sphere, in the laboratory frame. Both the radial  $B_r$  and the orthoradial  $B_\theta$  components are measured with a “Giant MagnetoResistance” (*GMR*) chip. The two chips are mounted on a circuit protected by a stainless steel tube. The probe has been installed at a latitude of  $50^\circ$ , as close as possible to the rotating sphere: the distance to the center of the sphere is about 22 cm. The variation of temperature has a significant effect on the measurements. Temperature is thus measured close to the *GMR* magnetometers, and a linear correction scheme is applied. The acquisition rate is 2000 samples per second, but all data presented here have been moving-averaged over 3 seconds, since we are focusing on the time-averaged axisymmetric mean flow.

### 3 Dimensionless numbers

Relevant parameters and dimensionless numbers are given in table 1. The symbols have their usual meaning :  $\eta$  is the magnetic diffusivity,  $\rho$  the density,  $\nu$  the kinematic viscosity of the liquid sodium. As in all moderate-size liquid sodium experiments, the Joule dissipation time  $\tau_J$  is relatively short. Since the imposed magnetic field is dipolar, its amplitude is much larger near the inner sphere ( $B = B_i$ ) than near the outer sphere ( $B = B_o$ ). We therefore evaluate those numbers that depend on the strength of the magnetic field in these two regions. The Hartmann number  $Ha$  is large everywhere. The Lundquist number  $S$  is large near the inner sphere, implying that Alfvén waves can play a role in the dynamics, with typical velocities  $U_a$  ranging from 0.2 to 5 m/s, in the same range as flow velocities.

Values of the Ekman number  $E$  are given for two typical values of the rotation rate  $f$  of the outer sphere. The *DTS* experiment has been designed for the

study of the magnetostrophic regime, in which Lorentz forces and Coriolis forces are of similar amplitude. This is measured by the Elsasser number  $\Lambda$ , which ranges from 0.01 near the outer sphere (where Coriolis forces dominate) to nearly 10 near the inner sphere (where Lorentz forces dominate). For time-scales short compared to the magnetic diffusion time, a measure of the relative influence of the rotational and magnetic effects is given by the dimensionless number  $\lambda$ , the ratio of the Alfvén velocity to the inertial wave velocity (Fearn et al., 1988; Cardin et al., 2002), which is called the Lehnert number (Lehnert, 1954) by Jault (2008). The Lehnert number is small in planetary cores, and rotational effects are expected to dominate at short time-scales. In the *DTS* experiment, the Lehnert number is less than 1.

We estimate a typical velocity  $U$  from the magnitude of the differential rotation  $\Delta f$  of the inner sphere with respect to the outer sphere. The estimate is based on the tangential velocity at the equator of the inner sphere. We will see that, because the magnetic coupling between the magnetized inner sphere and the liquid sodium is strong, velocities in the fluid layer typically reach this value. This yields magnetic Reynolds numbers  $Rm$  in excess of 40, while the Reynolds number  $Re$  lies in the range  $10^5 - 10^6$ . The interaction parameter  $N$  ranges from 0.01 near the outer sphere to 250 near the inner sphere, meaning that inertial effects only play a role near the outer boundary. Note that the Rossby number  $Ro$  is here simply defined as  $Ro = \Delta\Omega/\Omega = \Delta f/f$ .

The *DTS* experiment thus enables us to explore an original parameter range, which covers some aspects of liquid core dynamics.

## 4 Results

### 4.1 A typical run

Figure 3 illustrates the data typically acquired during a 1600s-long run. The top graph shows the variation of  $f$ , the rotation frequency of the outer sphere, and  $\Delta f$ , that of the inner sphere with respect to the outer sphere. The outer sphere is first set to a rotation rate of about 5 Hz, then several plateaux of different  $\Delta f$  are produced, down to  $\Delta f = -21.5$  Hz. Here, they all correspond to counter-rotation. Some small fluctuations of the rotation rates are observed ( $\pm 3\%$  max for  $\Delta f$  and  $\pm 7\%$  max for  $f$ ). They are due to variations in the power demanded to the motors, as shown in the next graph below, which displays the total power of the motors, reaching 2.3 kW. Note the large power fluctuations ( $\pm 22\%$ ) in the middle of the plateau with  $\Delta f = -19$  Hz. The next graph gives the differences in electric potential  $\Delta V$  recorded by the eight electrode pairs along a meridian. The highest signal reaches 3 mV. As

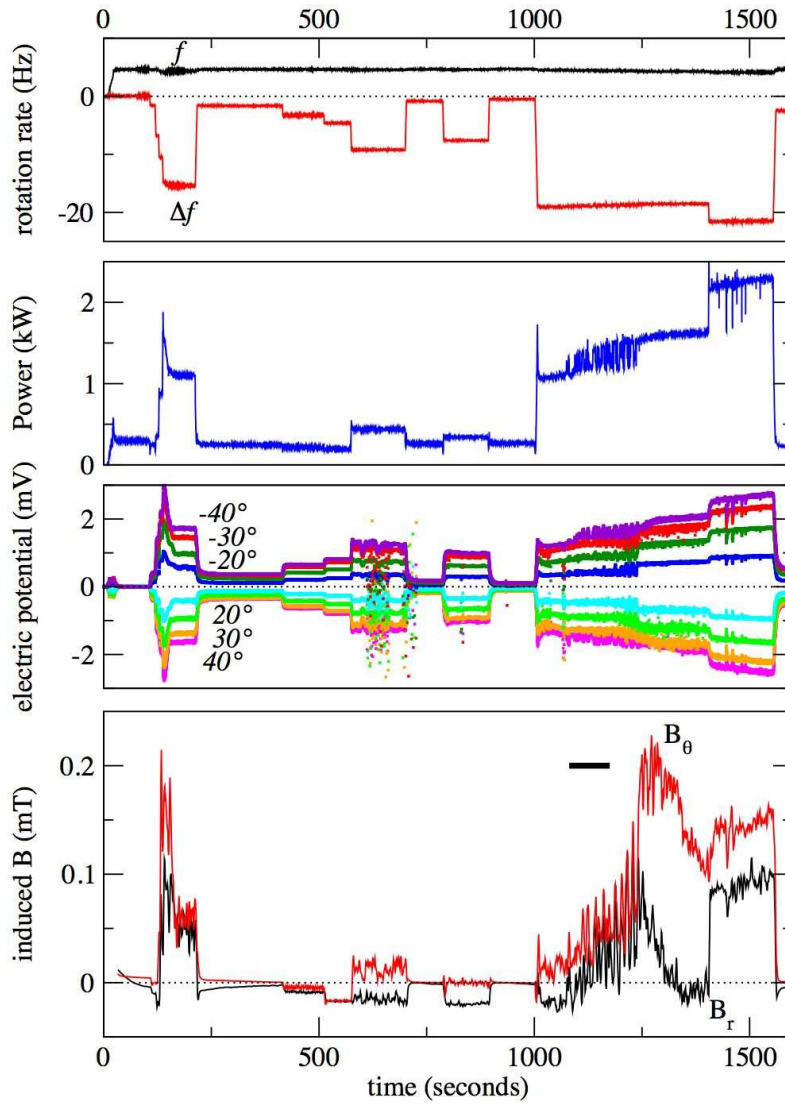


Fig. 3. An example of the data acquisition during an experimental run, as a function of time (in seconds). The top graph shows  $f$ , the rotation rate of the outer sphere, and  $\Delta f$ , the rotation rate of the inner sphere with respect to the outer sphere. The next graph below is the total power. The differences in electric potential recorded by the eight longitudinal electrode pairs (from  $-40^\circ$  to  $40^\circ$  latitude) is shown next. The last graph below gives the  $B_r$  and  $B_\theta$  components of the induced magnetic field (in mT) recorded on the  $50^\circ$ -latitude magnetometer, corrected for temperature. The horizontal bar in that graph gives the time window of the angular velocity record shown in figure 4.

symbol	expression	units	value			
$a$	outer radius	cm	21			
$b$	inner radius	cm	7.4			
$\tau_J$	$a^2/\pi^2\eta$	s	0.05			
			$B = B_i$		$B = B_o$	
Ha	$aB/\sqrt{\mu_0\rho\nu\eta}$		4400		210	
$S$	$aB/\eta\sqrt{\mu_0\rho}$		12		0.56	
$U_a$	$B/\sqrt{\mu_0\rho}$	m s <sup>-1</sup>	5.1		0.2	
			$f = 5\text{Hz}$		$f = 15\text{Hz}$	
E	$\nu/\Omega a^2$		4.7 10 <sup>-7</sup>		1.6 10 <sup>-7</sup>	
			$B = B_i$	$B = B_o$	$B = B_i$	$B = B_o$
$\Lambda$	$\sigma B^2/\rho\Omega$		9.2	0.02	3.1	0.01
$\lambda$	$U_a/a\Omega$		0.77	0.04	0.26	0.01
			$\Delta f = 0.5\text{Hz}$		$\Delta f = 40\text{Hz}$	
$U$	$b\Delta\Omega$	m s <sup>-1</sup>	0.23		18.6	
Rm	$Ua/\eta$		0.55		44	
Re	$Ua/\nu$		7 10 <sup>4</sup>		6 10 <sup>6</sup>	
			$B = B_i$	$B = B_o$	$B = B_i$	$B = B_o$
N	$\sigma a B^2/\rho U$		262	0.06	3.1	0.01

Table 1

Typical values of the relevant parameters and dimensionless numbers for different imposed rotation frequencies  $f = \Omega/2\pi$  of the outer sphere and differential rotation frequencies  $\Delta f = \Delta\Omega/2\pi$  of the inner sphere. For the numbers that depend on the magnetic field strength, two values are given, the first one with  $B = B_i = 0.175$  T at the equator of the inner sphere, the second one with  $B = B_o = 0.008$  T at the equator of the outer sphere.

expected from equation 2, the potential difference is largest at the highest latitude because  $B_r$  is largest there. Since  $\Delta f$  is negative, the electric potential differences are positive in the southern hemisphere and negative in the northern hemisphere (with our connection conventions). There is an almost perfect symmetry between the two hemispheres. Several ultrasonic Doppler velocity profiles are recorded during this sequence. The last graph below shows the induced magnetic field measured at 50° latitude. The records have been time-averaged along a 3 seconds-window to remove the fluctuations linked with the rotation of the outer sphere, and the imposed dipole contribution has been re-

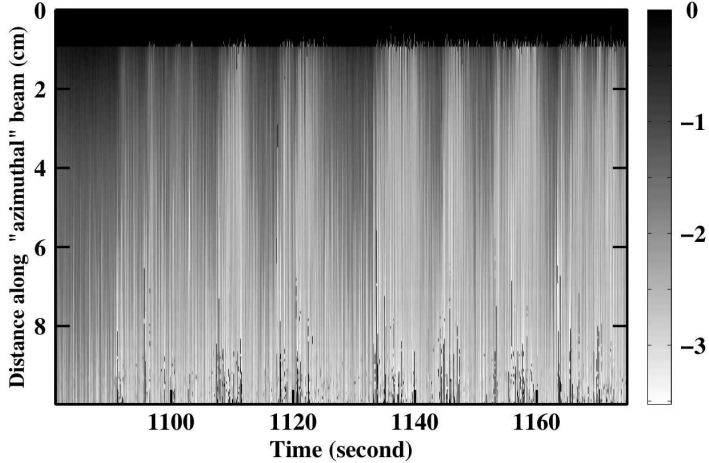


Fig. 4. An example of an ultrasonic Doppler angular velocity acquisition. The horizontal axis is time (in seconds) and the vertical axis is distance along the shooting line (in cm), here down to  $d \simeq 10$  cm. The corresponding time-window is drawn in figure 3. The shades give the velocity value in m/s (scale on the right-hand side). Strong velocity fluctuations are observed.

moved. The plateaux are well identified, but large fluctuations are observed when  $\Delta f$  is large. The maximum amplitude of the induced magnetic field is 0.23 mT (2.4% of the imposed field at this position).

A typical ultrasonic Doppler velocity record is shown in figure 4. It corresponds to the time window marked with a horizontal bar in the last graph of figure 3, when time-oscillations are observed on all data. The spatiotemporal plot clearly shows these oscillations. The velocities are largest at the bottom of the figure, where the ultrasonic beam gets closest to the inner sphere for this record. Equation 5 gives the value of the cylindrical radius  $s = 12.1$  cm. There, the velocity reaches -3.5 m/s. This large value is nevertheless smaller than the imposed tangential velocity on the inner sphere (-8.7 m/s). For this file, the time-interval between profiles is 15 ms, and there are 128 shots per profile. Velocities cannot be measured in the first 1 cm of the records, due to strong reverberations in the assembly wall.

Note that all data display large fluctuations in the time-window between 1100 and 1250 seconds. We will see that, in this parameter range, the flow exhibits a fundamental transition between two different configurations (see section 5.4). Here, this transition is preceded by large oscillations, while in some other runs, it occurs in one single step.

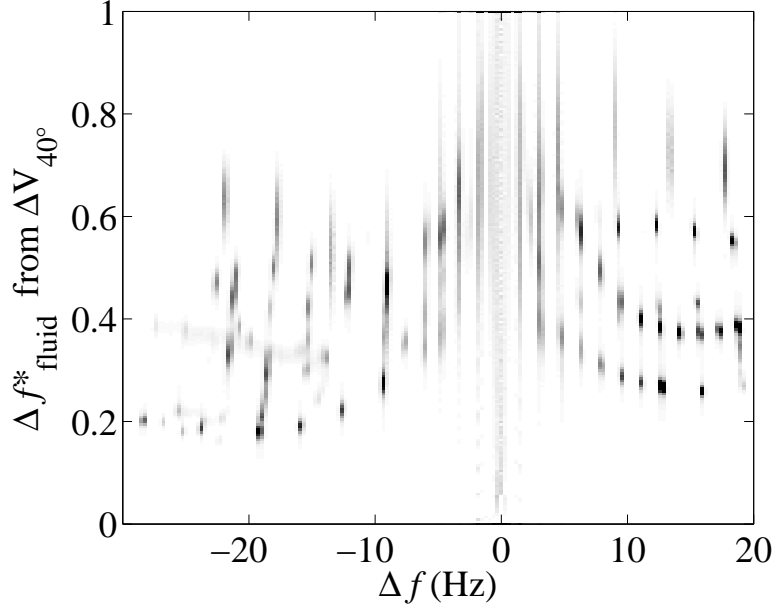


Fig. 5. A compilation of the variation of the normalized angular velocity of the liquid as a function of the imposed differential rotation rate  $\Delta f$ . The velocity of the outer sphere is  $f \simeq 4.5$  Hz for all data shown. The shades give the proportion of data points that yield a given couple of values. Note that very different angular velocities are measured for a given  $\Delta f$ .

#### 4.2 Evolution with the imposed differential rotation

Figure 5 shows the dimensionless angular frequencies  $\Delta f_{\text{fluid}}^* = U_\varphi / 2\pi s \Delta f$  deduced from the electric potential differences measured at  $40^\circ$  latitude (according to equation 2), as a function of the imposed differential rotation  $\Delta f$ , for a given rotation rate  $f \simeq 4.5$  Hz of the outer sphere. The figure is similar to figure 4 of Nataf et al. (2006), but data from several additional runs are included. The data points appear very scattered: for a given  $\Delta f$ , the dimensionless angular velocity can vary by up to a factor of 3. We think that this is due to variations in the electric coupling between liquid sodium and the inner copper sphere. The coupling between the rotating inner sphere and the liquid sodium depends on the electric currents that are induced in the sodium and loop in the copper inner sphere. A similar scatter is observed when plotting the induced magnetic field as a function of  $\Delta f$  (figure 6).

This scatter makes it difficult to draw robust conclusions about features such as super-rotation, but we will show in the next section that there is a linear relationship between the electric potential difference at  $40^\circ$  ( $\Delta V_{40^\circ}$ ) and the azimuthal velocities in the sodium actually measured with ultrasonic Doppler velocimetry. We will therefore use  $\Delta V_{40^\circ}$  as a proxy of the actual flow velocity, and we will see that several features of the flow become coherent when this

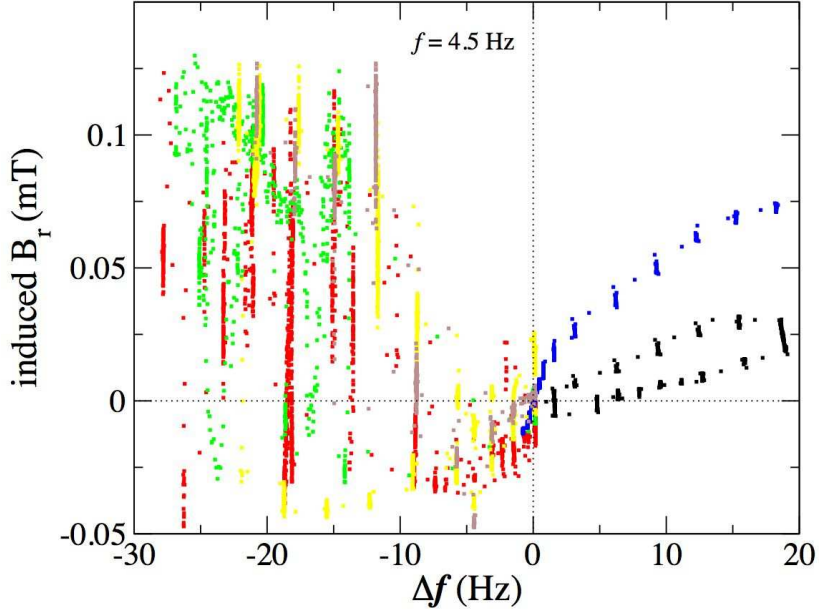


Fig. 6. A compilation of the variation of the radial component of the induced magnetic field as a function of the imposed differential rotation rate  $\Delta f$ . The velocity of the outer sphere is  $f \simeq 4.5$  Hz for all data shown. The colors indicate six different experimental runs. Note the large scatter of the data points, especially for negative  $\Delta f$ .

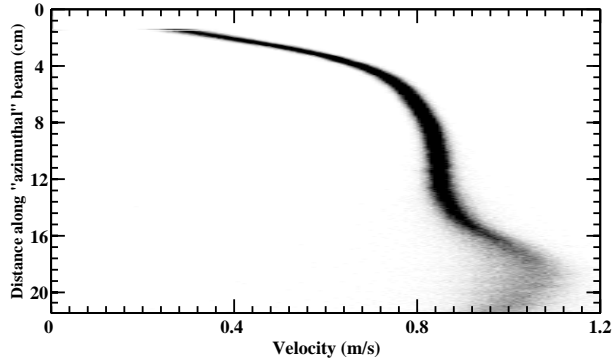


Fig. 7. Angular velocity profile for  $f = 4.7$  Hz and  $\Delta f = 4.8$  Hz. The time-interval between profiles is 30 ms, and there are 128 shots per profile. Probability density function or histogram of the velocity as a function of distance along shot.

proxy is used in place of  $\Delta f$ .

### 4.3 Angular velocity profiles

Using Doppler ultrasonic velocimetry, we are able to measure angular velocity of the liquid sodium flow. Figure 7 shows a profile of velocities measured along the shooting line for  $f = 4.7$  Hz and  $\Delta f = 4.8$  Hz. Equation 3 shows that

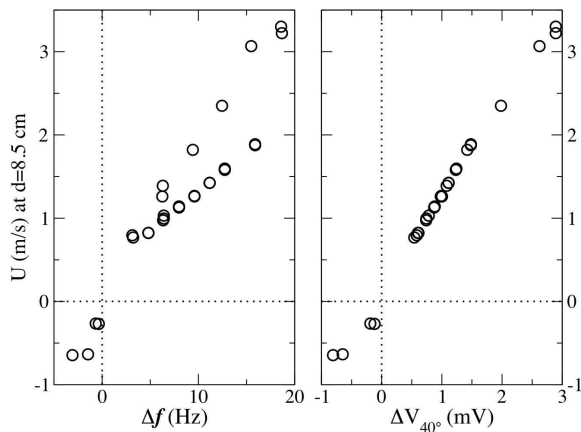


Fig. 8. Velocity (in m/s) at a distance of 8.5 cm along the shot line ( $s \simeq 13.6$ cm), as a function of  $\Delta f$  (left) and  $\Delta V_{40^\circ}$  (right). The rotation rate of the outer sphere is  $f \simeq 4.5$  Hz. The linear relation we get on the right shows that  $\Delta V_{40^\circ}$  is a good proxy of the angular velocity of the fluid at depth.

the measured velocity component is proportional to the angular velocity of the fluid. Actually, the plot is built from a 40 s-long record and the shades map the probability density function (*pdf*) of velocity versus distance. In this regime, the flow is almost steady and the *pdf* is sharp. Velocity rises steadily from a value close to 0.3 m/s at the outer boundary (top of the graph) to reach a plateau of about 0.85 m/s. The velocity further increases to a bump at 1.05 m/s where the ultrasonic beam gets closest to the inner sphere ( $d \simeq 18.8$  cm,  $s \simeq 7.9$  cm). We interpret this bump as the signature of the magnetic wind, which is confined to the neighborhood of the inner sphere, where the magnetic field is largest. The plateau characterizes the region where the fluid is entrained at an almost uniform angular velocity. This profile is typical of those measured when the outer sphere is rotating, and differs from those obtained when the outer sphere is at rest. For all available profiles, we pick the velocity measured at a distance of 8.5 cm (on the plateau, and about at mid-depth of the fluid layer, in the equatorial plane, according to figure 1) and plot it as a function of the corresponding  $\Delta f$  and  $\Delta V_{40^\circ}$  (Figure 8). While the former plot displays a large scatter, all points align well when velocity is plotted against  $\Delta V_{40^\circ}$ , illustrating the idea that the latter represents a good proxy of the effective velocity. From the regression line, we can translate  $\Delta V_{40^\circ}$  into fluid velocity or fluid flow frequency at depth in the fluid. We obtain:  $\Delta f_{\text{fluid}}/\Delta V_{40^\circ} \simeq 2600$  Hz/V. Note that the fluid velocity deduced from  $\Delta V_{40^\circ}$  using equation 2 agrees with the azimuthal velocity measured by ultrasonic Doppler velocimetry at the cylindrical radius corresponding to this latitude of  $40^\circ$ .

In figure 9, we have plotted all the profiles for  $f \simeq 4.5$  Hz and positive  $\Delta f$ , divided by the corresponding  $\Delta V_{40^\circ}$ . The horizontal scale has been chosen

to provide the actual adimensional angular velocity for the reference case  $\Delta f = 3.2$  Hz, according to equation 3. However, one should not consider this scale as universal, since the actual coupling is very variable (see figure 5). We have also drawn a synthetic profile derived from a numerical simulation similar to the one shown in figure 1 with  $\Delta f = 0.4$  Hz, but with the electric conductivity of the inner sphere reduced from its nominal value of 4.2 times that of the liquid sodium down to 0.04. In a first approximation, all experimental profiles collapse on a single curve, showing that the normalization with  $\Delta V_{40^\circ}$  is adequate. A closer look reveals that the rise of the velocity from the outer boundary is sharper when the forcing is weaker. In other words, the plateau of high angular velocity extends further towards the outer sphere for weak forcing. We will present in section 5.2 a simple model, in the spirit of Kleorin et al. (1997), that reproduces these characteristics (dotted and dashed lines). It seems that the relative size of the bump due to the magnetic wind above the plateau does not depend much upon the forcing. The comparison with the numerical profile suggests that the zone of strong magnetic wind is closer to the inner sphere in the experiments than in the simulation. We also note that the profile that corresponds to the highest differential rotation rate  $\Delta f = 18.7$  Hz plots below the others and has a distinct kink near the outer boundary, which makes it look more alike the profiles obtained with  $f = 0$ .

#### 4.4 Electric potentials

We showed in Nataf et al. (2006) that, when the outer sphere is at rest, the relative variation of electric potential differences (normalized to its value at  $40^\circ$ ) with latitude is independent of the differential rotation rate  $\Delta f$ . The better data now available confirm this observation and further demonstrate that the latitudinal variation of potentials is close to, but significantly different from, the one expected for solid body rotation. Figure 10 gives the variation of electric potential differences  $\Delta V$  at latitudes of  $10^\circ$ ,  $20^\circ$  and  $30^\circ$  as a function of  $\Delta V_{40^\circ}$ , for three different rotation rates of the outer sphere ( $f \simeq 4.5, 9$  and  $13.5$  Hz), and several different  $\Delta f$  (both positive and negative). The case with no rotation ( $f = 0$ ) is included for reference. In all four cases, the data points align well, and fall not far from (but distinctly off) the straight lines calculated for solid body rotation (*i.e.*, assuming  $U_\varphi$  proportional to  $s$  in equation 2). In fact, we deduce from the measured trend for  $f = 4.5$  Hz that the angular velocity at  $30^\circ$  is about 0.9 times that at  $40^\circ$ , in good agreement with the angular velocity profiles of figure 9. At lower latitudes, the apparent velocities deduced from the electric potentials are larger than the actual velocities, as the assumptions used in equation 2 break down (Nataf et al., 2006). In contrast with this simple linear trend, there is a distinct interval of  $\Delta V_{40^\circ}$  that displays a peculiar behavior, when the outer sphere is rotating. It occurs around  $\Delta V_{40^\circ} = -1.7$  mV for  $f = 4.5$  Hz,  $-3.3$  mV for  $f = 9$  Hz, and  $-4.4$  mV for  $f = 13.5$  Hz. The

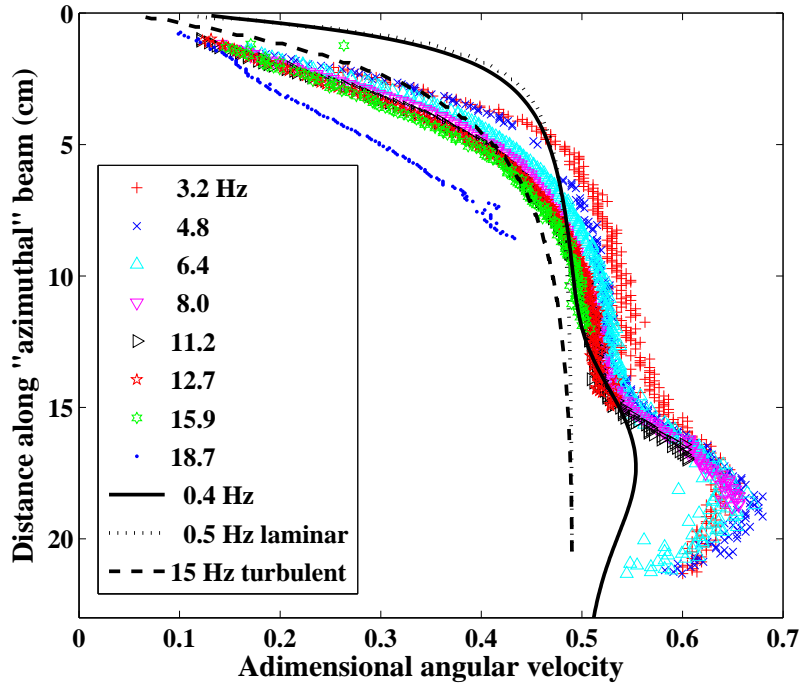


Fig. 9. A compilation of the angular velocity profiles, normalized by  $\Delta V_{40^\circ}$ , for  $f \simeq 4.5$  Hz and for imposed  $\Delta f$  ranging from 3.2 to 18.7 Hz. The horizontal scale has been chosen to give the actual adimensional angular velocity for the reference profile with  $\Delta f = 3.2$  Hz. The continuous lines are predictions of different sort: the solid line is the profile obtained from the numerical model of figure 1, ( $\Delta f = 0.4$  Hz) with the electrical conductivity of the inner sphere reduced by a factor 100 (see section 5.3). The almost superposed dotted line is derived from the analysis of Kleorin et al. (1997), and the dashed line is the prediction of our extended torque–balance model for  $\Delta f = 15$  Hz (see section 5.2). The two latter models only predict the shape of the boundary–layer profile, not the height of the plateau of near solid–body rotation.

kink means that, there, the variations in electric potentials are larger at low latitudes than at  $40^\circ$ . We will see below that the induced magnetic field also displays a very peculiar variation around the same values of  $\Delta V_{40^\circ}$ .

#### 4.5 Induced magnetic field

The induced magnetic field is measured outside the sphere, in the laboratory frame. The mean axisymmetric part of the induced field results from the interaction of the imposed axial dipolar magnetic field with the mean axisymmetric part of the meridional velocity field. The magnetometer signals are first averaged over 3 seconds, in order to remove the oscillatory part (which is discussed in another article (Schmitt et al., 2008)) and other magnetic perturbations. We

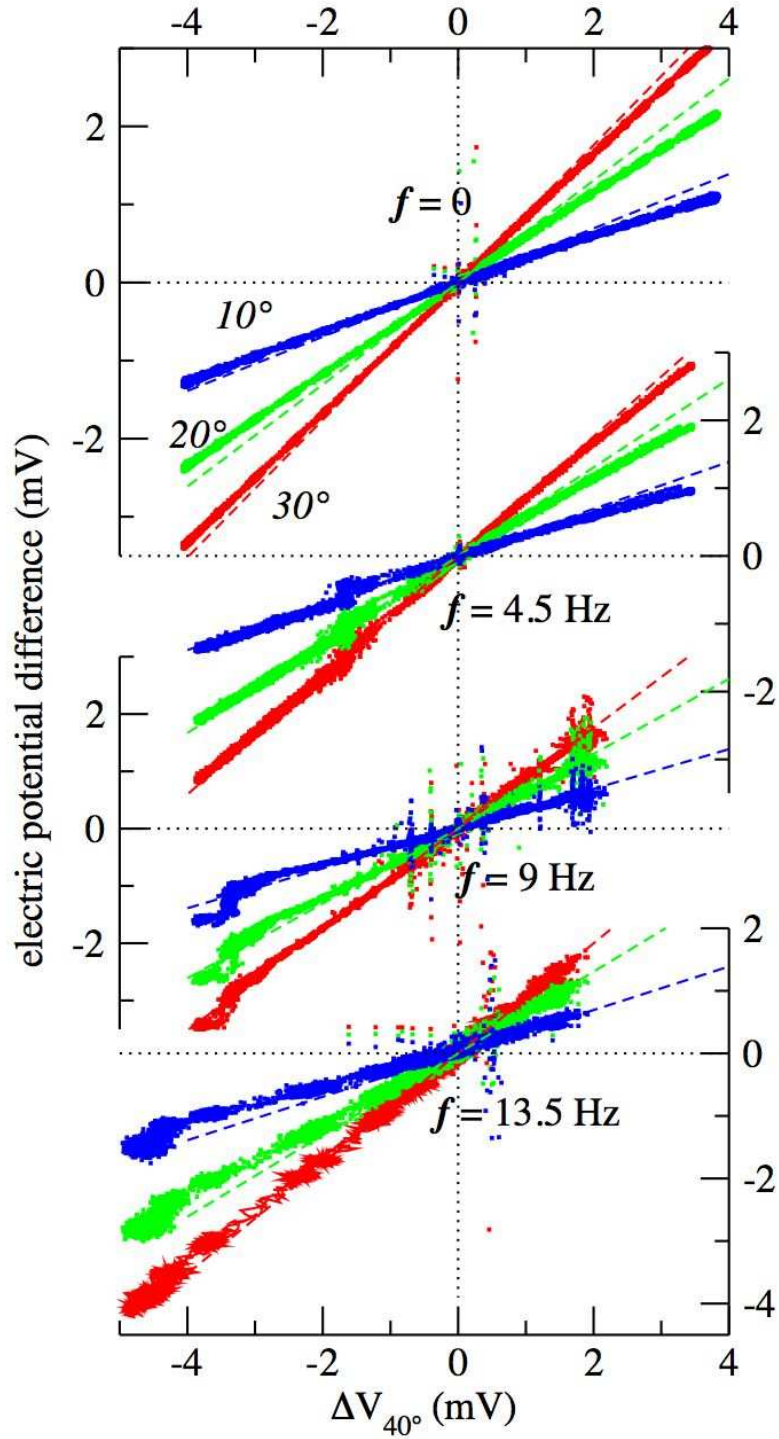


Fig. 10. A composite of electric potential differences for four different rotation rates  $f$  of the outer sphere. The electric potential difference measured at latitudes of  $10^\circ$ ,  $20^\circ$ , and  $30^\circ$  are plotted against that measured at  $40^\circ$ . The relation is almost linear, except for a kink observed around a negative value of  $\Delta V_{40^\circ}$ , which moves towards more negative values when  $f$  increases. The dashed straight lines indicate the relationship one would get if the fluid was in solid body rotation. Scattered points in the bottom panels are due to electromagnetic noise.

then correct for temperature drift, by removing an empirical linear correction. In figure 11, both the radial  $B_r$  and orthoradial  $B_\theta$  components are plotted as a function of  $\Delta V_{40^\circ}$  for several different imposed rotation frequencies  $f$  of the outer sphere. We have included the  $f = 0$  case for reference.

The first thing to note is the change of symmetry about  $\Delta V_{40^\circ} = 0$  for small forcing : while the induced magnetic field is always positive when the outer sphere is at rest, we find that the induced field has the sign of  $\Delta V_{40^\circ}$  (or  $\Delta f$ ) when the outer sphere is rotating. This can be directly related to the sense of the meridional circulation. When the outer sphere is at rest, the flow is always centrifugal in the equatorial plane, irrespective of the sign of  $\Delta f$ . When the outer sphere is rotating, the sense of the mass flux through the outer viscous boundary layer is governed by the sign of the differential rotation between the fluid and the outer sphere (as for Ekman pumping). When  $\Delta f/f$  is negative and small enough, the mass flux out of the boundary layer is thus centripetal at the equator.

In that same regime, we also note that the induced magnetic field is weaker when the outer sphere is rotating : the meridional circulation violates the Proudman–Taylor constraint and therefore decreases as the Ekman number decreases (see figure 6 of Hollerbach et al. (2007)).

However, the most interesting feature of the curves shown in figure 11 is the distinctive narrow peak observed at negative  $\Delta f$  (here negative  $\Delta V_{40^\circ}$ ). The peak occurs for a value of  $\Delta V_{40^\circ}$  that moves toward more negative values as  $f$  increases. In fact, the occurrence of the peak corresponds to the transition between two different regimes, which was invoked when discussing figure 10. We stress that it is because we plot the induced magnetic field as a function of  $\Delta V_{40^\circ}$  rather than  $\Delta f$  that we obtain a well defined and reproducible peak (compare with figure 6). The peak happens as the flow evolves from centripetal to centrifugal in the equatorial plane, as the effect of differential rotation takes over the effect of global rotation.

#### 4.6 Radial velocity profiles

While the induced magnetic field measured outside the sphere is a good indicator of the global symmetries of the meridional flow, it cannot be used to investigate the internal organization of that flow. Here, we add the information brought by radial profiles of the radial velocity obtained by ultrasonic Doppler velocimetry. A compilation of the profiles obtained for three different rotation frequencies  $f$  of the outer sphere is given in figure 12 for two different latitudes:  $-20^\circ$  (figure 12a) and  $-40^\circ$  (figure 12b). The profiles clearly confirm that the sign of the radial velocity changes with the sign of  $\Delta f$ , as inferred from the

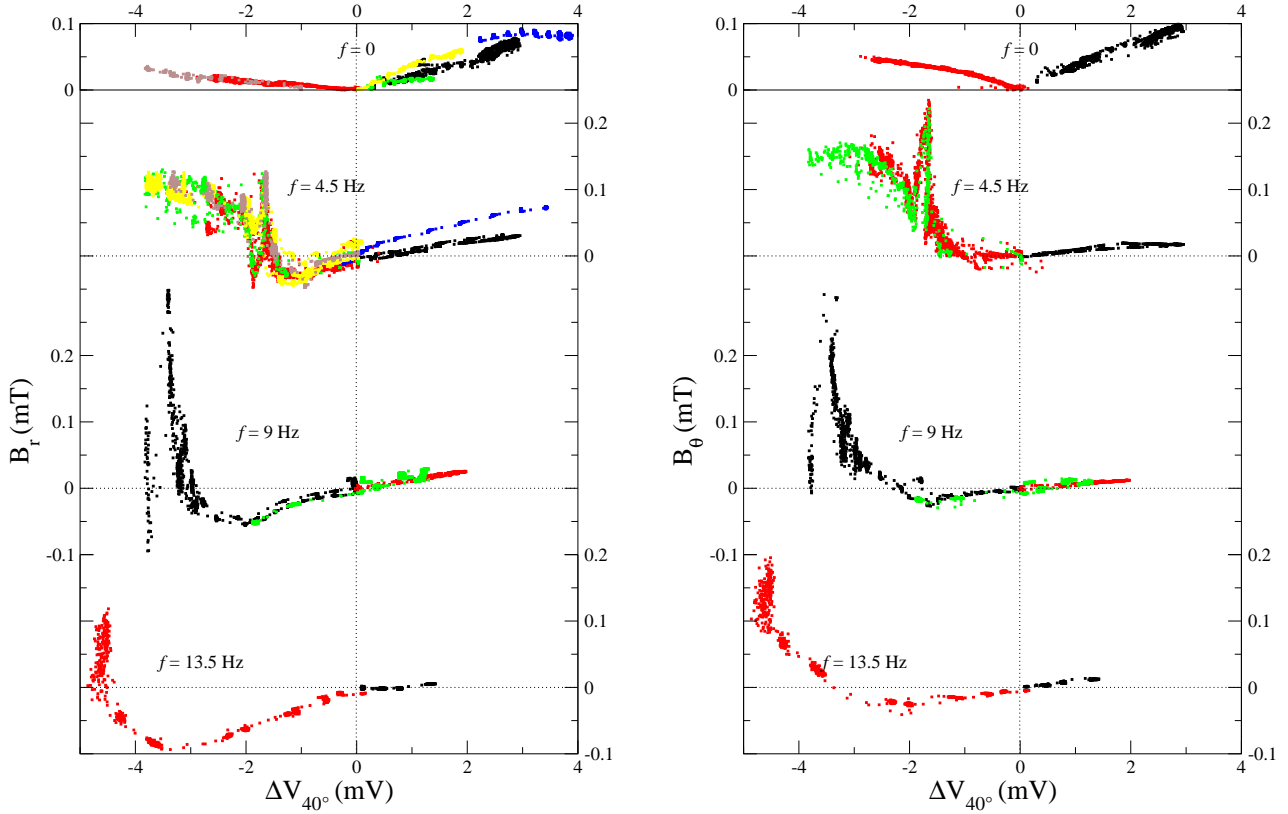


Fig. 11. A composite of the induced magnetic field as a function of  $\Delta V_{40^\circ}$ , for four different rotation frequencies  $f$  of the outer sphere. Radial component on the left, and orthoradial component on the right. Note the symmetry change around the origin ( $\Delta f \simeq 0$ ) between the case without rotation ( $f = 0$ ) and the other cases. A striking peak is observed for a particular value of  $\Delta f$  in the counterrotating regime ( $\Delta V_{40^\circ} < 0$ ). The colors correspond to different runs.

induced magnetic field measurements. At  $-40^\circ$ , the profiles are characterized by a broad peak with radial velocity rising from zero at the inner sphere to a maximum, which can reach about 3% of the tangential velocity of the inner sphere. There, the flow is centripetal when the Rossby number is positive. The radial velocity falls back to zero at nearly the same radius for all  $f$ , but the profiles for the higher  $f$  (lower Ekman number) are characterized by a strong second peak. At  $-20^\circ$ , the amplitudes are similar but seem to increase with  $f$ . The change of sign as  $\Delta f$  changes sign is well visible again.

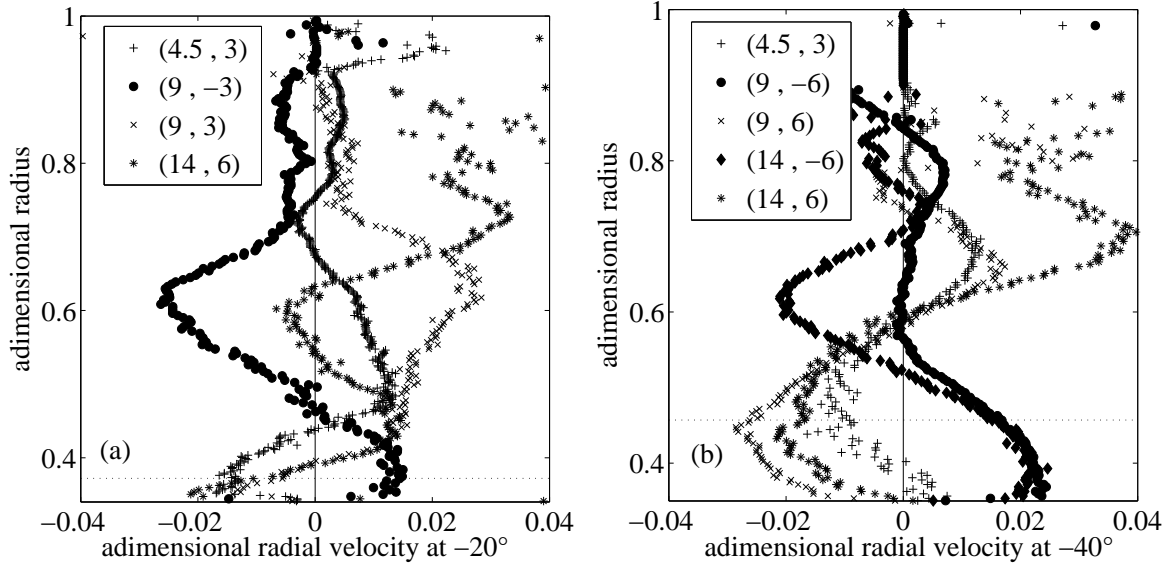


Fig. 12. Radial velocity, obtained by ultrasonic Doppler velocimetry, as a function of adimensional radius (vertical axis) at two different latitudes:  $-20^\circ$  (a) and  $-40^\circ$  (b). The dotted line indicates the radius of the tangent cylinder on the inner sphere, whose adimensional radius is 0.35 (bottom of the plots). All velocities are normalized with the differential tangential velocity at the equator of the inner sphere. The profiles are labelled by their  $(f, \Delta f)$  pair. Note that the sign of the radial velocity changes as the sign of  $\Delta f$ , as expected for Ekman–pumping dominated flow.

## 5 Discussion and conclusions

### 5.1 Moderate–Rossby number regime

The magnetostrophic regime at moderate Rossby numbers is characterized by a low level of turbulence. Most of the energy is in the axisymmetric mean flow described in this article. The meridional circulation has the symmetry of Ekman pumping: counterclockwise in a meridional plane (*i.e.*, centrifugal at the equator) for  $Ro > 0$  and clockwise for  $Ro < 0$ . Radial velocities are at least one order of magnitude smaller than azimuthal velocities. Waves are observed in this regime, and are described in another article (Schmitt et al., 2008).

Profiles of the angular velocity of the flow have been obtained, using ultrasonic Doppler velocimetry. They reveal a region where magnetic wind is present, near the inner sphere, where the magnetic field is largest. Farther away, the flow is geostrophic, under the effect of the Coriolis force. A large part of the geostrophic region is entrained by the magnetic wind at a nearly constant angular velocity.

The measurements show that the shape of the angular velocity profile is nearly independent of  $Ro$  as long as it remains moderate. This suggests that, in contrast to the case with a fixed outer sphere (Nataf et al., 2006; Hollerbach et al., 2007), the linear solution ( $Ro \ll 1$ ) provides a good description of the flow. We were able to compute solutions in the linear regime with the geometry and parameters of the *DTS* experiment for  $f = 5$  Hz ( $E = 4.7 \cdot 10^{-7}$ ), as shown in figure 1. In figure 1a, one clearly sees a non-geostrophic inner region where the Ferraro law of isorotation applies, a central part where the flow is geostrophic and in almost solid-body rotation, and an outer domain, which is also geostrophic but in which the angular velocity decreases rapidly towards the outer sphere. In order to compare with the experimental results, synthetic velocity profiles have been computed. The comparison of the angular velocity profiles is shown in figure 9. All profiles show the plateau of nearly constant angular velocity, the central peak due to the magnetic wind, and the gentle drop to lower velocity towards the outer sphere. We note however that this velocity drop is much steeper in the numerical simulation (which has  $Ro = 0.08$ ). Several of these features had been predicted by Kleeorin et al. (1997) in an asymptotic study of spherical Couette flow in a dipolar magnetic field. We recall their main results below and propose an extension of their approach, which better explains our experimental results.

### 5.2 *Modified Taylor constraint and extended quasi-geostrophic model for the moderate-Rossby number flow*

The quasi-geostrophic regime with an imposed magnetic field has been studied extensively by Kleeorin et al. (1997). Following the pioneer computations of Hollerbach (1994) of rotating spherical Couette in a dipolar magnetic field, they worked out the asymptotic solutions for small Elsasser, Ekman, Reynolds and Rossby numbers. They predicted the existence of a geostrophic region where the magnetic torque on coaxial cylindrical tubes balances weak friction in the upper and lower Ekman layers, thus providing an extension of the zero-Ekman number analysis of Taylor (1963), which results in the so-called Taylor-state. We consider the torques at work on a cylindrical tube at cylindrical radius from  $s$  to  $s + ds$ . Neglecting the volumetric viscous friction (small Ekman number), the torque balance can be written as:

$$d\gamma_T(s) + d\gamma_B(s) + d\Gamma_M(s) = 0, \quad (6)$$

where  $d\gamma_T$  and  $d\gamma_B$  are the (resistive) torques on the top and bottom spherical caps at the outer sphere, and  $d\Gamma_M$  is the volumetric (driving) torque exerted by the Lorentz force (magnetic torque). In our case, the surface torques are

due to Ekman friction on the outer sphere and can be written:

$$d\gamma_T(s) = d\gamma_B(s) = 2\pi s^2 \tau_V \frac{ds}{\cos \theta}, \quad (7)$$

where  $\theta$  is the colatitude and  $\tau_V$  is the azimuthal component of the friction stress on the outer shell.

At high latitudes, friction in the Ekman layers is weak and, as in the Taylor state, the balancing magnetic torque vanishes in the steady-state and the fluid is in solid body rotation. The magnetic torque can be expressed as:

$$d\Gamma_M(s) = 2\pi s^2 ds \int_{z_B}^{z_T} (\vec{j} \times \vec{B})_\varphi dz = \frac{2\pi}{\mu_0} ds \frac{d}{ds} \left[ s^2 \int_{z_B}^{z_T} B_s b_\varphi dz \right], \quad (8)$$

where  $B_s$  is the component of the imposed magnetic field along the cylindrical radius  $s$ , while  $b_\varphi$  is the (unknown) azimuthal component of the induced magnetic field. This component results from the shearing of the dipolar field lines by deviations of the fluid flow from solid body rotation. A weak magnetic torque thus implies a small deviation from solid body rotation, especially where the imposed field  $B_s$  is large, *i.e.* near the inner sphere (but not too close, because the flow is no longer geostrophic there). As noted by Kleorin et al. (1997), this explains why the angular velocity of the fluid  $\Delta\omega(s)$  is almost constant in the central part of the spherical shell. The progressive decrease of the angular velocity as  $s$  increases further was predicted by Kleorin et al. (1997). In this layer, which they call “magnetic–Proudman”, shear in the upper and lower Ekman layers increases, so as to produce a large enough  $b_\varphi$  to compensate for the decrease of  $B_s$  in the expression of the magnetic torque. In order to be more quantitative, one needs to express  $b_\varphi(s, z)$  as a function of  $\Delta\omega(s)$ . Kleorin et al. (1997) show that, when the imposed magnetic field is a dipole, the magnetic torque can be written:

$$d\Gamma_M(s) = \frac{12\pi}{\mu_0\eta} B_0^2 a^5 \Delta\Omega \frac{ds}{a} \left[ 2 \left( 1 - \frac{s}{a} \right) \right]^{3/2} \frac{\Delta\omega^\dagger - \Delta\omega(s)}{\Delta\Omega}, \quad (9)$$

where  $\Delta\omega^\dagger$  is the differential rotation of the fluid in the region of nearly solid-body rotation. The friction stress for the laminar Ekman layer is easily calculated and yields:

$$d\gamma_T(s) = -2\pi\rho a^4 \Delta\Omega \sqrt{\nu\Omega} \frac{ds}{a} \frac{s^3}{a^3} \left[ 1 - \frac{s^2}{a^2} \right]^{-1/4} \frac{\Delta\omega(s)}{\Delta\Omega}. \quad (10)$$

Injecting expressions 9 and 10 in equation 6 in the boundary layer approximation ( $s \simeq a$ ), Kleorin et al. (1997) obtain the shape of the profile of the angular velocity versus  $s$ :

$$\Delta\omega(s) = \frac{\Delta\omega^\dagger}{1 + \frac{\rho\sqrt{\nu\Omega}}{3a\sigma B_0^2} \left[2 \left(1 - \frac{s}{a}\right)\right]^{-7/4}} \quad (11)$$

The synthetic angular velocity profile derived from this expression is the dotted line of figure 9. The value of  $\Delta\omega^\dagger$  has been chosen to coincide with the full numerical profile drawn (solid line). Indeed, Kleorin et al. (1997) studied the case when the flow remains geostrophic all the way to the inner sphere, where they matched the solid-body solution to the Stewartson layer modified by the magnetic field. They could thus predict the value of  $\Delta\omega^\dagger$ . In our case, the inner region is not geostrophic, and we only use their analysis to probe the shape of the angular velocity profiles in the geostrophic region. It is clear that, in that region, the asymptotic prediction of Kleorin et al. (1997) is a very good approximation of the actual numerical profile. However, we note that both profiles fail to explain the much more gentle rise of angular velocity observed in the experiments. The explanation is that the Ekman boundary layer becomes turbulent at the high  $\Delta f$  reached in our experiments. We can retain the approach of Kleorin et al. (1997) and simply allow for turbulent friction stress  $\tau_V$  in equation 7. Because of turbulence, Ekman friction is enhanced and a stronger magnetic torque is needed to balance it. This results in a widening of the ‘‘Proudman–magnetic’’ layer, as shown by the dashed line in figure 9, computed for  $\Delta f = 15$  Hz. The widening increases as  $\Delta f$  increases, in excellent agreement with our measurements. The full ingredients and implications of this extended model will be given elsewhere.

### 5.3 Variable electric coupling and $Ro_{eff}$

In Nataf et al. (2006), there were hints that different flows could be obtained for the same imposed rotation rates  $f$  and  $\Delta f$ . Our new data confirm this trend. We speculate that this behavior is due to variations in the electric coupling between liquid sodium and the copper inner sphere, under the effect of electrowetting feedback. It is thus difficult to relate the observed signals to the imposed  $\Delta f$ , as we would like to do in order to study the possibility for the magnetic wind to induce super-rotation of the fluid as in Dormy et al. (1998). However, we find that most results can be cast in a coherent frame if we use  $\Delta V_{40^\circ}$ , the electric potential difference at latitude  $40^\circ$ , as a proxy of the actual angular velocity, in place of  $\Delta f$ , resulting in an effective Rossby number  $Ro_{eff}$ . In order to mimic a weaker electric coupling, numerical simulations have been run where the electric conductivity of the inner sphere is

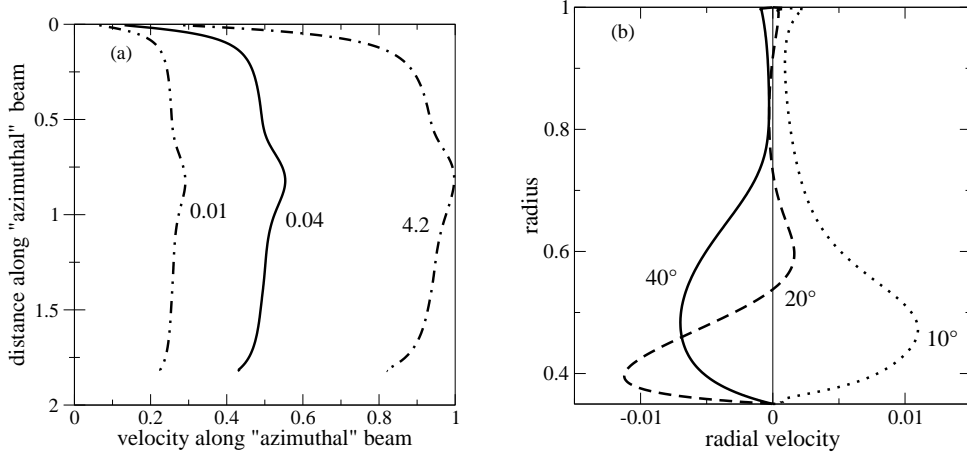


Fig. 13. Synthetic Doppler velocity profiles computed from numerical simulations. (a) angular velocity synthetics for a shot from the azimuthal assembly at  $10^\circ$  (see projected raypath in figure 1a). The synthetics take into account the finite width of the ultrasonic beam and the projection of the meridional velocity. The dash-dot line is for the numerical simulation of figure 1, in which the electric conductivity of the inner sphere is 4.2 times that of the liquid sodium, as expected for copper. The other computations have a reduced inner sphere conductivity ratio of 0.01 (dot-dot-dash), and 0.04 (solid line). The corresponding angular velocity profile for the latter is also drawn in figure 9. (b) radial velocity synthetics for radial shots at latitudes  $\pm 40^\circ$ ,  $\pm 20^\circ$  and  $\pm 10^\circ$  for the latter model. Velocities are normalised with the differential tangential velocity at the equator of the inner sphere, and distances are normalised by the radius of the outer sphere.

reduced as compared to that of copper (nominal conductivity ratio of 4.2). Synthetic angular velocity profiles are shown in figure 13a for a conductivity ratio of 0.04 and 0.01. The profiles retain the same shape but the overall amplitude is severely reduced. This explains why we could get coherent results by renormalizing all data with the  $\Delta V_{40^\circ}$  proxy. Comparing the spread in figure 5 with the numerical simulations suggests that the effective conductivity at the sodium/copper interface could be reduced by as much as 100 by wetting problems. We observe that the electric coupling deteriorates with time over the months, but that it can be somewhat revived by letting the copper in contact with liquid sodium at  $150^\circ\text{C}$  during 3 days.

The numerical simulations show that the meridional circulation is not very sensitive to the conductivity ratio. Radial profiles of the radial velocity are shown in figure 13b for the numerical model with the conductivity ratio of 0.04. As in figure 1b, the circulation is centrifugal at the equator ( $Ro > 0$ ) and the radial velocity is positive at the latitude of  $10^\circ$ . It is negative at  $-40^\circ$ , in good agreement with our measurements (figure 12b). At  $20^\circ$ , the profile is more complex, but it is also negative near the inner sphere, as experimentally observed (figure 12a). In the numerical model, the radial velocities reach about 1% of the inner sphere tangential velocity, while it is about twice as large in the

experiments. The experiments show clear evidence of a secondary meridional cell farther away from the inner sphere.

#### 5.4 *The peculiar regime for $Ro_{eff} \simeq -1$*

In the counter-rotating case, the centripetal circulation at the equator, which characterizes the moderate Rossby number regime, transforms into a centrifugal circulation at the equator as the Rossby number increases. We recall that at small Rossby number, the meridional circulation is governed by Hartmann-pumping at the inner sphere, and is therefore directed towards the inner sphere when it is counter-rotating, while centrifugation from the inner sphere takes over at large Rossby numbers. The transition between the two regimes occurs over a narrow interval of  $\Delta V_{40^\circ}$ , and is marked by a peak of the induced magnetic field. This happens where the effective angular velocity of the fluid is such that it almost cancels that of the outer sphere, as seen in the laboratory frame.

Our interpretation is that, in a narrow window of  $\Delta V_{40^\circ}$ , the antagonistic effects of the rotation of the outer and inner spheres drive the liquid in a state that shows almost no rotation with respect to the laboratory frame. The constraint of rotation then vanishes, and a vigorous meridional circulation is allowed, resulting in an enhanced induced magnetic field.

Some support for this interpretation is given by a direct measurement of the angular velocity using the ultrasonic Doppler technique. As shown in figure 14, a peculiar profile is measured close to the  $B$  peak. An almost uniform angular velocity is measured (down to  $d \simeq 7.4$  cm, i.e. at mid-depth of the fluid shell). Using equation 3, we find a fluid rotation frequency of -5.7 Hz on this plateau. Since the ultrasonic probe is installed in the rotating sphere, the angular velocity with respect to the laboratory frame is obtained by adding the angular velocity of the outer sphere. The resulting angular velocity is then  $-5.7 + 4.2 = -1.5$  Hz, which is small but non zero. Note that the electric potentials (figure 10) also suggest that, on and beyond the peak, the fluid is nearly in solid-body rotation. However, the above scenario is probably too simple, and the variation of the induced magnetic field calls for a more sophisticated interpretation. For example, the  $B_r$  and  $B_\theta$  records of figure 3 show that the ‘‘centrifugal’’ regime is announced by a strong rise of  $B_\theta$ , while  $B_r$  starts decreasing instead. Besides, pure solid-body rotation would imply no meridional circulation altogether.

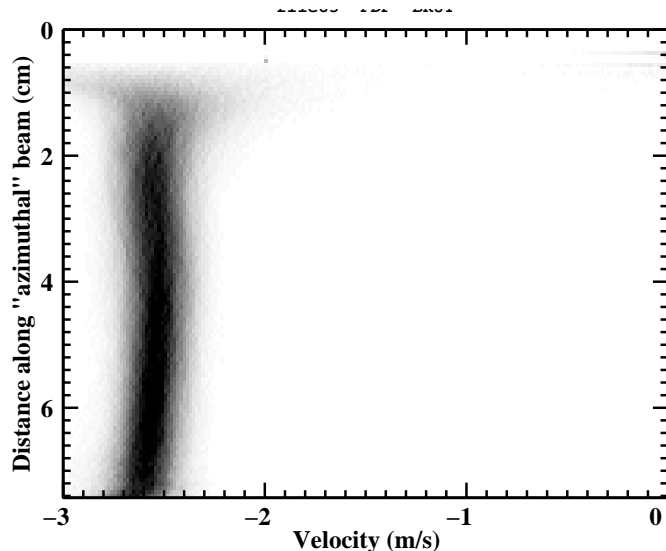


Fig. 14. A profile (*pdf*) of the angular velocity of the fluid for  $f = 4.2\text{Hz}$  and  $\Delta f = -18.2\text{Hz}$ , for which  $\Delta V_{40^\circ} = -1.7\text{mV}$ . This value corresponds to the peak observed for the induced magnetic field.

### 5.5 Implications for experimental dynamos

The transition between the centripetal and the centrifugal regimes deserves a specific discussion in the context of the preparation of experimental dynamos. In Cardin et al. (2002), we evaluated the possibility to run a dynamo where the forcing is a rotating spherical Couette flow. Such a dynamo would run in the magnetostrophic regime, expected for planetary cores, and it would be of the  $\alpha\omega$ -type, displaying large azimuthal magnetic fields. However, the critical magnetic Reynolds number  $\text{Rm}_c$  for these dynamos appears to be high (Schaeffer and Cardin, 2006). Indeed, there is an optimum ratio of meridional to azimuthal velocities that yield a minimum  $\text{Rm}_c$  (Ravelet et al., 2005; Bayliss et al., 2007). Here, we find that, in a rapidly rotating spherical Couette flow, the meridional velocities are at least one order of magnitude smaller than the azimuthal velocities. In contrast, the mean flow in other experiments (Peffley et al., 2000; Ravelet et al., 2005; Bayliss et al., 2007) is tuned to be close to an axi-symmetric flow of the Dudley and James (1989) family, with a strong meridional circulation, yielding an  $\alpha^2$ -dynamo, and moderate  $\text{Rm}_c$  (Kumar and Roberts, 1975; Dudley and James, 1989). It has been recently suggested that the dynamo efficiency of such flows can be significantly reduced by turbulent fluctuations (Bayliss et al., 2007). Now, in the narrow window that corresponds to the transition from the centripetal regime to the centrifugal regime, the magnitude of the meridional circulation becomes comparable to the azimuthal one. Thus, the value of the magnetic Reynolds number for the onset of dynamo action may be minimum around this transition. A rotating

spherical Couette flow dynamo experiment should thus make it possible to observe the transition from an  $\alpha^2$ -type (with  $\text{Rm}_c$  perhaps large compared to its laminar value) to an  $\alpha\omega$ -type dynamo (with a large  $\text{Rm}_c$  for the laminar flow but weak turbulent effects). We are currently conducting extensive numerical simulations of the dynamo instability for spherical Couette flow to document this effect.

### 5.6 Implications for core dynamics

The modified Taylor state observed in the *DTS* experiment bears some relevance to the expected dynamical regime in the Earth's core. Indeed, the Ekman number based on the expected fluid viscosity is very small, but observations of the nutations reveal that the friction at the core–mantle boundary is some  $10^4$  larger than expected for linear Ekman friction (Herring et al., 2002; Koot et al., 2008). Although the origin of this enhanced friction is still debated (Deleplace and Cardin, 2006; Buffett and Christensen, 2007) and is undoubtedly different from the turbulent friction present in *DTS*, it would be worth investigating its effect on the dynamics of the core, from a modified Taylor state point of view. Quasi-geostrophic numerical models (Schaeffer and Cardin, 2006), in which Ekman friction is parameterized, are a particularly attractive tool for quantifying this effect.

## Acknowledgments

We thank Jean-Paul Masson and Patrick La Rizza for their skillful technical assistance, and Alexandre Fournier for useful discussions. We are indebted to two anonymous reviewers whose comments helped us improving the manuscript. The *DTS* project is supported by Fonds National de la Science, Institut National des Sciences de l'Univers, Centre National de la Recherche Scientifique, Région Rhône-Alpes and Université Joseph Fourier. This research benefited from an invitation of HCN and DJ at the KITP, Santa Barbara, and was thus supported in part by the USA National Science Foundation under Grant No. PHY05-51164.

## References

Bayliss, R. A., Forest, C. B., Nornberg, M. D., Spence, E. J., Terry, P. W., Feb. 2007. Numerical simulations of current generation and dynamo excitation in a mechanically forced turbulent flow. *Physical Review E* 75 (2), 026303–+.

- Braginsky, S. I., Meytlis, V. P., 1990. Local turbulence in the Earth's core. *Geophysical and Astrophysical Fluid Dynamics* 55, 71–87.
- Brito, D., Nataf, H.-C., Cardin, P., Aubert, J., Masson, J.-P., 2001. Ultrasonic Doppler velocimetry in liquid gallium. *Experiments in Fluids* 31, 653–663.
- Buffett, B., Christensen, U., 2007. Magnetic and viscous coupling at the core–mantle boundary: inferences from observations of the Earth's nutations. *Geophys. J. Int.* 171, 145–152.
- Buffett, B. A., Jun. 2003. A comparison of subgrid-scale models for large-eddy simulations of convection in the Earth's core. *Geophysical Journal International* 153, 753–765.
- Cardin, P., Brito, D., Jault, D., Nataf, H.-C., Masson, J.-P., 2002. Towards A Rapidly Rotating Liquid Sodium Dynamo Experiment. *Magnetohydrodynamics* 38, 177–189.
- Deleplace, B., Cardin, P., 2006. Viscomagnetic torque at the core–mantle boundary. *Geophys. J. Int.* 167, 557–566.
- Dormy, E., Cardin, P., Jault, D., Jul. 1998. MHD flow in a slightly differentially rotating spherical shell, with conducting inner core, in a dipolar magnetic field. *Earth and Planetary Science Letters* 160, 15–30.
- Dormy, E., Jault, D., Soward, A. M., 2002. A super-rotating shear layer in magnetohydrodynamic spherical Couette flow. *J. Fluid Mech.* 452, 263–291.
- Dudley, M. L., James, R. W., Oct. 1989. Time-dependent kinematic dynamos with stationary flows. *Royal Society of London Proceedings Series A* 425, 407–429.
- Eckert, S., Gerbeth, G., 2002. Velocity measurements in liquid sodium by means of ultrasound Doppler velocimetry. *Experiments in Fluids* 32, 542–546.
- Fearn, D. R., Roberts, P. H., Soward, A. M., 1988. Convection, stability and the dynamo. In: Galdi, G. P., Straughan, B. (Eds.), *Energy Stability and Convection*. Longman scientific and technical Harlow, pp. 60–324.
- Ferraro, V. C. A., 1937. The non-uniform rotation of the sun and its magnetic field. *Month. Notices Roy. Astr. Soc.* 97, 458–472.
- Herring, T., Mathews, P., Buffett, B., 2002. Modeling nutation and precession: very long baseline interferometry results. *J. Geophys. Res.* 107B, 145–152.
- Hollerbach, R., 1994. Magnetohydrodynamic Ekman and Stewartson layers in a rotating spherical shell. *Proc. R. Soc. Lond. A* 444, 333–346.
- Hollerbach, R., 2000. Magnetohydrodynamic flows in spherical shells. In: Egbers, C., Pfister, G. (Eds.), *LNP Vol. 549: Physics of Rotating Fluids*. pp. 295–+.
- Hollerbach, R., Canet, E., Fournier, A., Feb. 2007. Spherical Couette flow in a dipolar magnetic field. *European J. Mech. Fluids* 26, 729–737.
- Jault, D., 2008. Axial invariance of rapidly varying diffusionless motions in the Earth's core interior. *Physics of the Earth and Planetary Interiors* 166, 67–76.
- Kelley, D. H., Triana, S. A., Zimmerman, D. S., Tilgner, A., Lathrop, D. P., 2007. Inertial waves driven by differential rotation in a planetary geometry.

- Geophysical and Astrophysical Fluid Dynamics 101, 469–487.
- Kleorin, N., Rogachevskii, I., Ruzmaikin, A., Soward, A. M., Starchenko, S. V., 1997. Axisymmetric flow between differentially rotating spheres in a dipole field. *J. Fluid Mech.* 344, 213–244.
- Koot, L., Rivoldini, A., de Viron, O., Dehant, V., 2008. Estimation of Earth interior parameters from a Bayesian inversion of VLBI nutation time series. *Journal of Geophysical Research*, in press.
- Kumar, S., Roberts, P. H., 1975. A Three-Dimensional Kinematic Dynamo. *Royal Society of London Proceedings Series A* 344, 235–258.
- Lehnert, B., May 1954. Magnetohydrodynamic Waves Under the Action of the Coriolis Force. *Astrophysical Journal* 119, 647–+.
- Matsui, H., Buffett, B. A., 2007. Commutation error correction for large eddy simulations of convection driven dynamos. *Geophysical and Astrophysical Fluid Dynamics* 101, 429–449.
- Nataf, H.-C., Alboussière, T., Brito, D., Cardin, P., Gagnière, N., Jault, D., Masson, J.-P., Schmitt, D., Oct. 2006. Experimental study of super-rotation in a magnetostrophic spherical Couette flow. *Geophysical and Astrophysical Fluid Dynamics* 100, 281–298.
- Peffley, N. L., Goumivlevski, A. G., Cawthorne, A. B., Lathrop, D. P., Jul. 2000. Characterization of experimental dynamos. *Geophysical Journal International* 142, 52–58.
- Ravelet, F., Chiffaudel, A., Daviaud, F., Léorat, J., Nov. 2005. Toward an experimental von Kármán dynamo: Numerical studies for an optimized design. *Physics of Fluids* 17, 7104–+.
- Schaeffer, N., Cardin, P., May 2006. Quasi-geostrophic kinematic dynamos at low magnetic Prandtl number. *Earth and Planetary Science Letters* 245, 595–604.
- Schmitt, D., Alboussière, T., Brito, D., Cardin, P., Gagnière, N., Jault, D., Nataf, H.-C., 2008. Rotating spherical Couette flow in a dipolar magnetic field: Experimental study of magneto-inertial waves. *Journal of Fluid Mechanics* 604, 175–197.
- Sisan, D. R., Mujica, N., Tillotson, W. A., Huang, Y.-M., Dorland, W., Hassam, A. B., Antonsen, T. M., Lathrop, D. P., Sep. 2004. Experimental Observation and Characterization of the Magnetorotational Instability. *Physical Review Letters* 93 (11), 114502–+.
- St. Pierre, M. G., 1996. On the local nature of turbulence in Earth’s outer core. *Geophysical and Astrophysical Fluid Dynamics* 83, 293–306.
- Starchenko, S. V., 1998. Magnetohydrodynamic flow between insulating shells rotating in strong potential field. *Physics of Fluids* 10, 2412–2420.
- Stewartson, K., 1966. On almost rigid rotations. Part 2. *Journal of Fluid Mechanics* 26, 131–144.
- Taylor, J., 1963. The magneto-hydrodynamics of a rotating fluid and the Earth’s dynamo problem. *Proc. R. Soc. Lond. A* 274, 274–283.